

# Drift-Diffusion Studies of Compositional Morphology in Bulk Heterojunctions: The Role of the Mixed Phase in Photovoltaic Performance

Benjamin Y. Finck\* and Benjamin J. Schwartz†

*Department of Chemistry and Biochemistry, University of California,  
Los Angeles, California 90095-1569, USA*

(Received 31 May 2016; revised manuscript received 8 September 2016; published 18 November 2016)

The active layers of most organic photovoltaic (OPV) devices are constructed from a blend of two organic compounds. The two materials spontaneously segregate into pure-component phases during device fabrication, creating a bicontinuous network of conduction pathways that are selective for electron or hole charge carriers. The morphological distribution of these materials within the active layer has long been known to influence charge transport and resulting device performance. In addition to the two pure-component phases present in these devices, a third, mixed-composition phase exists at the interface between the two pure phases. The exact effects of this mixed-composition phase on OPV device performance are not well understood, although it is argued that the presence of a mixed phase is necessary for optimal device operation. In this paper, we probe the effects of having a mixed-composition interfacial phase on the performance and charge-transport characteristics of OPV devices through a series of drift-diffusion model simulations. We start with set of model morphologies with only pure-component phases and then introduce an interfacial mixed phase in a controllable fashion. Our simulations show that a modest amount of mixing initially improves device efficiency by reducing the tortuosity of the device's conduction pathways and easing morphological traps. However, an excessive amount of mixing can actually degrade high-conductivity pathways, reducing photovoltaic performance. The point at which mixing switches from being beneficial to detrimental to OPV performance depends on the average domain size of a device's morphology. Devices with smaller feature sizes are more susceptible to the debilitating effects of overmixing, so that the presence of a mixed phase may either raise power-conversion efficiency by as much as 100% or lower it by as much as 50%, depending on the average domain size and the extent of mixing. These trends suggest that variations in the amount of mixed-composition phase with different processing conditions is one of the key factors that makes optimizing bulk heterojunction OPV devices difficult.

DOI: 10.1103/PhysRevApplied.6.054008

## I. INTRODUCTION

In recent years, photovoltaic devices based on organic materials, referred to as OPVs, have made major gains in their efficiency. Single-junction OPVs have surpassed 10% power-conversion efficiency (PCE) [1], and multijunction tandem devices have achieved efficiencies up to 12% [2]. The majority of organic photovoltaic devices are based on a binary blend of a semiconducting polymer and a fullerene derivative. The polymer serves as the light absorber producing excitons. To split the excitons into free carriers and generate electrical current, such polymers are paired with an electron acceptor, typically a fullerene derivative. These two materials are usually blended together and processed into an approximately 100-nm-thick film that is layered between two electrodes. The charge carriers then migrate to their respective electrodes by traveling through pathways constructed from their preferred conducting molecules (electrons through the fullerene and holes

through the polymer). Efficient charge transport is contingent upon the two conducting materials forming a bicontinuous network so that the charges may move through the device unimpeded. This mix of donor and acceptor materials within the active layer of the OPV device to facilitate both exciton separation and subsequent charge transport is known as a bulk heterojunction (BHJ) [3–5].

The way in which excitons are split and carriers are transported in a BHJ makes the performance of OPV devices highly sensitive to the kinetics of how the active organic layer is processed [4,6,7]. Because charge carriers travel selectively through the electron donor and acceptor molecules, it is evident that the structural details of an OPV device's internal morphology have a profound effect on charge transport and, thus, a device's photovoltaic performance. Further complicating the matter is that the binary component blend used in BHJs results in an active layer with three distinct compositional phases: pure polymer domains, pure fullerene domains, and an amorphous mixed-composition interfacial domain that must lie between the pure-component domains. There is debate within the OPV community about how both the relative

\*bfinck@chem.ucla.edu

†schwartz@chem.ucla.edu

sizes of these three domains and the way they are distributed affect OPV device performance. In particular, some have argued that the mixed-composition regime is crucial to OPV device operation, since charge generation occurs most prevalently near the interface between the donor and acceptor molecules [8–10]. Insufficient fullerene intercalation into amorphous polymer domains can result in morphological electron traps, emphasizing the need for sufficiently intermixed regions in the BHJ [11]. Conversely, excessive mixing between fullerene and polymer can result in higher rates of charge recombination, which can lower device performance [12]. Moreover, excitons generated in BHJ devices typically have diffusion lengths of approximately 10 nm, which is comparable to the average domain size of many polymer or BHJ devices [8,13]. A recent kinetic Monte Carlo study by Jones *et al.* [14] suggested that the presence of a mixed phase is detrimental to device performance. However, that study considered only binary phase morphologies with pure donor and acceptor domains or with pure fullerene aggregates suspended in a mixed phase and not the three-phase morphologies that many BHJs exhibit. Thus, it is not immediately clear to what degree the presence of a mixed-composition domain is beneficial or detrimental to optimum OPV operation.

There are two main reasons why it is difficult to determine if a mixed amorphous phase is necessary for OPV operation, and if so, how much is needed and how it should be distributed relative to the pure-component phases. First, there is no easy experimental method for controlling the relative amounts or spatial distribution of different phases in an OPV active layer because the morphology is determined primarily by the kinetics of how the film is processed [3,7]. This kinetic sensitivity means that none of the experimental “knobs” that can be tuned (e.g., the use of solvent additives during spin coating [15], post-treatment via solvent [16], thermal annealing [17], etc.) can be used to controllably change the relative amounts of phase separation and/or mixed-phase region in an active layer made from a given set of materials. Second, morphological characterization of the different organic components in OPVs via electron microscopy is problematic, primarily due to the low contrast between typical OPV materials. Only a few papers have attempted to actually quantify the relative amounts of the single-component phases and the mixed phase [18–20] and then only for a few selected configurations of a very limited set of materials.

All of these complications have hampered experimental efforts to probe the effects of OPV morphology and the presence or absence of a mixed phase on device performance. Thus, in this paper, we utilize semiconductor device modeling to address this question, focusing our efforts on the well-known drift-diffusion (DD) model [21–24]. Several groups have used the DD approach to study the effects of morphology and morphological disorder on OPV

performance [24–29]. There are two types of disorder to consider, which although interrelated, can affect OPV device performance in different ways: energetic disorder, which results from twists and kinks within the polymer chains or other changes in the local environment that produce different energetics for different sites in the active-layer film, and structural disorder, which results from the tortuosity of the bicontinuous network that can lead to “dead ends” and other morphological features that are nonoptimal for carrier transport. Many studies have examined the effects of energetic disorder on OPV performance, usually assuming a Gaussian distribution of energetic states and/or an exponential tail of trap states in 1D drift-diffusion simulations [30,31]. Other groups have focused on the impact of structural disorder and morphological features by performing 2D drift-diffusion simulations to study the effects of phase separation and component arrangement on device performance [26,28,29,32,33]; we also have presented a 1D method for examining structural disorder based on DD simulations of ensembles of 1D devices with position-dependent mobility profiles [34].

In this paper, we present a set of 2D drift-diffusion simulations specifically designed to probe the effects of the presence of a controllably varied mixed-composition, interfacial phase on device performance. We begin by utilizing morphologies generated by Cahn-Hilliard (CH) modeling of binary fluid phase separation, as has been employed successfully in previous 2D DD modeling studies of OPVs [28,29]. The CH morphologies allow us to tune the component domain sizes with a single parameter, and we then introduce an interfacial mixed region between the pure-component regions by smoothing the binary morphology in a continuously controllable fashion. To verify that the conclusions drawn from these artificial morphologies also apply to real BHJ morphologies, we also utilize a single empirical morphology obtained via high-angle annular dark-field scanning transmission electron microscopy (HAADF STEM), whose pure donor, pure acceptor, and mixed-phase domains have been previously characterized [35]. We then map charge-carrier mobilities to both the CH- and HAADF-STEM-generated morphologies, allowing us to probe the effects of having differing amounts of mixed-composition interfacial domains present in BHJ OPV devices at various average morphological feature sizes.

From our simulations, we find that the presence of interfacial mixed regions can be either beneficial or deleterious to OPV device performance depending on the average pure-domain feature size and the amount of mixed phase introduced. This is somewhat in contrast to the conclusions of Jones *et al.* [14], who asserted that the presence of a mixed phase should hinder only device performance. We find that introducing a mixed phase can improve device performance by reducing the number

of morphological traps (i.e., dead ends or “cul-de-sacs”) and reducing the tortuosity of conduction pathways. In some cases, the introduction of a mixed phase even creates new conduction pathways by connecting previously disjointed conduction domains. However, excessive mixing eventually reduces device performance by degrading conduction pathways along the pure components, resulting in poorer charge transport and increased loss of carriers to recombination. The point at which mixing becomes deleterious, rather than beneficial, to charge transport differs depending on the average feature size of the simulated morphology. These conflicting influences result in non-monotonic trends for device performance as a function of the degree of mixing and the average domain size. The nonmonotonic effects of the presence of the mixed phase on device performance may explain why it is experimentally so laboriously difficult to optimize new donor-acceptor pairings and why OPV device performance is so sensitive to processing conditions.

## II. COMPUTATIONAL METHODS

### A. Drift-diffusion model

For this work, we perform our device simulations using the drift-diffusion model of electrical current, in which the electron and hole current densities ( $J_n$ ,  $J_p$ ) are assumed to take the functional form [36]

$$J_n = -qn\mu_n\nabla V + k_B T\mu_n\nabla n, \quad (1)$$

$$J_p = -qp\mu_p\nabla V - k_B T\mu_p\nabla p, \quad (2)$$

where  $q$  is the fundamental charge,  $n$  and  $p$  refer to electron and hole densities, respectively,  $V$  is the electrostatic potential,  $T$  is the temperature,  $k_B$  is Boltzmann’s constant, and  $\mu_n$  and  $\mu_p$  refer to the mobility of electrons and holes, respectively [37]. In order to simulate a working device, one must solve the density continuity equations for both carriers,

$$\frac{\partial n}{\partial t} = \frac{1}{q}\nabla \cdot J_n - R + G, \quad (3)$$

$$\frac{\partial p}{\partial t} = -\frac{1}{q}\nabla \cdot J_p - R + G, \quad (4)$$

where  $R$  is the recombination rate, and  $G$  is the generation rate of electrons and holes. Because the literature consensus is that recombination events in OPV devices are trap-assisted processes, we follow the approach of previous groups and use the following functional form of Shockley-Read-Hall recombination with an exponential distribution of trap states [30,31]. The rate of recombination via conduction-band tail states is given by

$$R_{\text{CBT}} = \int_{E_V}^{E_C} \frac{N_{C_0} \exp\left(\frac{E-E_C}{E_{\text{UC}}}\right) (np - n_i^2)}{\frac{n+N_C \exp\left(\frac{E-E_C}{E_{\text{UC}}}\right)}{\beta_p^-} + \frac{p+N_V \exp\left(\frac{E_V-E}{E_{\text{UC}}}\right)}{\beta_n^0}} dE,$$

where  $N_{C_0}$  is the density of tail states at the conduction-band edge,  $E_{\text{UC}}$  is the Urbach energy which defines the exponential decay of tail states,  $N_{C/V}$  are the effective density of states at the conduction or valence bands, and  $n_i$  is the intrinsic carrier concentration. The capture rate coefficients  $\beta_p^-$  and  $\beta_n^0$ , which are the product of the thermal velocity and the capture cross sections of electrons and holes, represent the rate of capture of holes by trapped negatively charged conduction-band states and of electrons by unoccupied conduction-band states, respectively. A similar expression exists for recombination via valence-band tail states  $R_{\text{VBT}}$ . The full recombination rate is given by the sum of these two recombination rates,  $R = R_{\text{CBT}} + R_{\text{VBT}}$ . To appropriately account for the thin-film interference effects that occur in normal OPV device layer structures, we use a transfer-matrix formalism [38] to calculate the absorption profile and also allow for the carrier generation profile to be morphology dependent, as discussed in Sec. II B 3.

Once generated, the carrier densities must also satisfy the Poisson equation

$$\nabla^2 V = \frac{q}{\epsilon_r \epsilon_0} (n - p), \quad (5)$$

where  $V$  is the electrostatic potential,  $\epsilon_r$  is the dielectric constant of the active medium, and  $\epsilon_0$  is the vacuum permittivity. This additional requirement means that all of the above equations are inherently coupled. The set of Eqs. (1)–(5) forms the basis of the DD model.

We use the Gummel method to decouple the above set of partial differential equations and solve them numerically in an iterative manner [39]. Equations (3)–(5) are appropriately discretized and solved on 2D finite-difference mesh [36,40,41]. Boundary conditions at the semiconductor-metal contacts are treated as Dirichlet type, meaning the values of the carrier densities and potential are predetermined. For the boundary conditions for the carrier densities at the electrodes, we assume thermionic injection of free carriers from the metals into the organic semiconducting materials of the active layer [42]. For the Poisson equation’s boundary conditions, we assume that the potential drop across the device is equal to the built-in voltage,  $V_{\text{BI}}$ . The lateral boundary conditions are treated as Neumann type, meaning the gradients of ( $n$ ,  $p$ , and  $V$ ) are predetermined. We set the gradients of these variables to zero at the sides of the device, since there should not be excessive lateral drift or diffusion current for reasonably wide active areas like those explored here. Collectively, the boundary conditions for our DD simulations are

$$n(x, 0) = N_C \exp\left(-\frac{\Phi_{B,\text{ano}}}{kT}\right), \quad (6)$$

$$n(x, d) = N_C \exp\left(-\frac{\Phi_{B,\text{cat}}}{kT}\right), \quad (7)$$

$$p(x, 0) = N_V \exp\left(-\frac{E_g - \Phi_{B,\text{ano}}}{kT}\right), \quad (8)$$

$$p(x, d) = N_V \exp\left(-\frac{E_g - \Phi_{B,\text{cat}}}{kT}\right), \quad (9)$$

$$V(x, 0) = 0, \quad (10)$$

$$V(x, d) = V_{\text{BI}}, \quad (11)$$

$$\frac{\partial n(0, y)}{\partial x} = \frac{\partial n(w, y)}{\partial x} = 0, \quad (12)$$

$$\frac{\partial p(0, y)}{\partial x} = \frac{\partial p(w, y)}{\partial x} = 0, \quad (13)$$

$$\frac{\partial V(0, y)}{\partial x} = \frac{\partial V(w, y)}{\partial x} = 0, \quad (14)$$

where  $\Phi_{B,\text{ano/cat}}$  are the Schottky barriers at the anode or cathode,  $N_{C/V}$  are the density of chargeable sites or vacancies for electrons or holes,  $E_g$  is the effective band gap represented by the offset between the polymer's HOMO and the fullerene's LUMO, and  $d$  and  $w$  refer to the depth and width of the simulated device. The dimensions of most of our simulated devices are chosen to be 100 nm deep by 300 nm wide. We believe that a cross section of this width provides an active area large enough to capture the majority of morphological effects of the average feature sizes ( $< 15$  nm) studied here, while small enough to be computationally tractable. We choose additional simulation parameters that are comparable to those previously used in the literature [31,43]. All the parameters pertinent to our calculations are collected in Table I.

## B. Mapping morphologies to a DD OPV device model

### 1. Cahn-Hilliard-generated morphologies

There has been relatively limited direct nanometer-scale compositional mapping of OPV active layers due to the limited contrast between typical donor and acceptor components [18–20] and we discuss performing DD simulations with experimental morphologies further below. But to fully understand the interplay between the average domain size and the degree of mixing in OPV device performance, we choose to start with a series of computer-generated binary component morphologies (i.e., containing only pure phases and no mixed phase) of varying average domain

TABLE I. Boundary conditions and values of other parameters used for all the DD simulations presented in this work, except where otherwise noted in the text.

Parameter	Symbol	Value
Active-layer depth	$d$	100 nm
Active-layer width	$w$	300 nm
Relative permittivity	$\epsilon_r$	3.5
Schottky injection barriers	$\phi_n, \phi_p$	0.4, 0.1 eV
Electron mobility in acceptor	$\mu_{n,A}$	$10^{-7} \text{ m}^2 \text{ V}^{-1} \text{ s}^{-1}$
Electron mobility in donor	$\mu_{n,D}$	$10^{-12} \text{ m}^2 \text{ V}^{-1} \text{ s}^{-1}$
Hole mobility in acceptor	$\mu_{p,A}$	$10^{-12} \text{ m}^2 \text{ V}^{-1} \text{ s}^{-1}$
Hole mobility in donor	$\mu_{p,D}$	$10^{-8} \text{ m}^2 \text{ V}^{-1} \text{ s}^{-1}$
Built-in voltage	$V_{\text{BI}}$	0.7 V
Density of trap states	$N_C, N_V$	$1 \times 10^{20} \text{ cm}^{-3}$
Urbach energy	$E_{\text{UC}}, E_{\text{UV}}$	40 meV
Capture rate coefficient	$\beta_{n,p}^{+,-,0}$	$1 \times 10^{13} \text{ cm}^{-3} \text{ s}^{-1}$
Temperature	$T$	298 K
Band gap	$E_g$	1.2 eV

size and then introduce a mixed-phase interfacial domain with a controllably varying width.

We follow the approach of several previous groups and generate an initial series of model morphologies based on the spontaneous phase separation of a binary fluid mixture. This approach involves solving the CH equation

$$\frac{\partial C}{\partial t} = D \nabla^2 (C^3 - C - \epsilon \nabla^2 C), \quad (15)$$

where  $C$  is the spatial composition of the fluid mixture that ranges from one pure component to the other [ $C(x, y) \in [0, 1]$ ]. In this equation,  $D$  is the diffusivity, and  $\epsilon$  is the interfacial interaction energy between the two components. Since our primary interest in Cahn-Hilliard morphologies is the semirandom distribution of phases at differing length scales, we set  $D = 1$  and instead vary only the relative interaction energy. Since the interaction energy determines the average domain size of the resulting morphologies, this single parameter allows us to simulate bulk heterojunction morphologies with a controllably varying average feature size. We employ Eyre's linearly stabilized Cahn-Hilliard integration scheme [44,45] to solve the Cahn-Hilliard equation on a 2D grid, an approach that has previously been applied to generate polymer-fullerene BHJ morphologies [28,29].

Although other Cahn-Hilliard-based studies have investigated morphology characteristics such as average feature size [46], annealing time (represented by the CH integration time) [28], and tortuosity on OPV device performance [47], for this study, we are primarily interested in the effects of the amorphous mixed-composition interfacial regions and how such regions may be important for BHJs to function. Thus, we choose to start with a few base morphologies that have feature sizes of approximately 4, 8, 10, 12, and 15 nm (we determine the average feature size via examination of

TABLE II. Boundary conditions and parameters used for the CH binary fluid simulations, except where otherwise noted in the text. All values serve as unitless parameters for the simulations. The average domain sizes of the morphologies generated with these parameters are given in the last row of this table.

Parameter	Symbol	Value
Diffusivity	$D$	1
Simulation time	$t_{\max}$	1000
Time step	$\Delta t$	0.5
Interaction energy	$\epsilon$	0.0018, 0.0023, 0.0024, 0.0025, 0.0030
Average domain size of generated morphologies		4, 8 nm 10, 12, 15 nm

pair-pair distribution functions for each morphology) [48]. To this end, we simulate all our morphologies using identical starting parameters, which are listed in Table II, except for the interaction energy  $\epsilon$  that determines the average domain size.

It is worth noting that the morphologies generated by Cahn-Hilliard simulation necessarily have an interfacial width that is related to the domain size. However, in real BHJs, the mechanics of local phase separation are more complicated, since most BHJ phase separation is driven by polymer crystallization and/or agglomeration of the fullerene, which may not be well represented by the simple separation of immiscible fluids. Thus, the interfacial regions generated in CH morphologies may not correspond well with the mixed regions found in real BHJs with a comparable average feature size. To account for possible discrepancies between CH and actual BHJ interfacial domain size and to gain more control over our simulated mixed interfacial regions, we start by completely binarizing our CH morphologies (i.e., rounding  $C$  to either 0 or 1 at every point in space), thus, generating morphologies with only pure-component domains. We then reintroduce mixed regions by “blending” the pure domains at the interface by successively applying Gaussian smoothing operations. This method results in a morphology that varies from 0 to 1 with a smooth interface of varying and controlled width between the pure domains. In this way, we can explore the OPV performance of active layers that have amorphous interfacial regions of varying dimension for BHJs with different active-layer feature sizes. An example of a binarized Cahn-Hilliard morphology and the effects of our Gaussian smoothing procedure on this morphology are shown in Figs. 2(a) and 2(c).

We note that this method of Gaussian smoothing to “mix” the pure phases introduces only a mixed phase at the interface between pure regions. The amount of mixed region introduced by a smoothing operation is, thus, dependent on the fraction of the device that can be characterized as lying near an interface. Because the initial CH morphologies that we explore have different feature sizes, they also have different amounts of interface in their

initial compositions so that applying a single Gaussian smoothing operation to the different morphologies does not introduce the same amount of mixed phase. In order to easily compare the effects of mixing between different feature-sized morphologies, we instead choose to use the standard deviation  $\sigma$  of the morphologies’ compositions as a way to quantify the degree of mixing. In the completely unmixed morphologies, all mesh points have a composition value of 0 or 1, since we have only pure regions. Since the mole fraction ratio of donor to acceptor is 0.5, the standard deviation in composition of the initial morphology is 0.5. In contrast, if we construct a perfectly blended homogeneous morphology, all mesh points should have the same compositional value of 0.5, leading to a standard deviation of exactly zero. The standard deviation values between these two limits, thus, provide a measure of the fraction of the morphology that is mixed, as quoted in the caption to Fig. 2. Thus, we define the fraction of the device that is mixed  $f_{\text{mixed}}$  from the standard deviation of the device’s composition  $\sigma$  by

$$f_{\text{mixed}} = 1 - 2 \times \sigma. \quad (16)$$

## 2. Empirical (HAADF STEM) morphology

As previously discussed, it is not clear how well Cahn-Hilliard-generated morphologies are representative of the BHJ morphologies in actual OPV devices. The CH formalism is an idealized model of binary fluid phase separation, but the phase separation kinetics of typical OPV donor-acceptor blends is significantly more complicated than that of ideal immiscible fluids [3,4,6,7]. Therefore, in addition to the artificial CH morphologies that we simulate, we also simulate an experimental morphology that is well characterized in terms of its compositional domain distribution [18].

The particular experimental morphology we simulate, presented in Fig. 3(a), is taken from Ref. [18], which used HAADF STEM to determine the compositional density profile of donor and acceptor materials, specifically, poly-3-hexylthiophene (P3HT) and the endohedral metallofullerene 1-[3-(2-ethyl)hexoxy carbonyl]propyl-1-phenyl-Lu3N@C<sub>80</sub>. In their analysis, the authors of Ref. [18] were able to specifically characterize the experimentally observed compositional domains as pure donor, pure acceptor, or mixed. For our simulations, we represent the local composition  $C(x, y)$  with 1 corresponding to pure acceptor, 0 to pure donor, and 0.5 to the mixed region. To determine the device’s average domain size with its pair-pair distribution function, we examine the morphology without the mixed phase and determine that the average feature size of the pure domains is approximately 26 nm, which is notably coarser than any of our CH morphologies. For this particular 2D slice of this experimental morphology, the mixed-component domain accounts for 16% of the device’s active

area, using Eq. (16) for quantifying the degree of mixing. We then utilize this compositional data to map out the charge-carrier generation profile, which we set to occur only in the mixed-component region and which we base on the calculated light absorption profile determined by solving a transfer-matrix formalism to account for thin-film interference effects, as described in Sec. II B 4. We also use the local composition to determine the local charge-carrier mobilities, as we discuss in more detail in Sec. II B 3

### 3. Mapping morphology to simulated device parameters

With our set of morphologies in hand, the next step is to incorporate these morphologies into our drift-diffusion simulator. The device parameters that should be most directly affected by the compositional morphology are the mobilities and generation rate of charge carriers. The two organic components typically used in BHJ solar cells are often charge-carrier selective in regards to their mobility. For example, the archetypal OPV polymer P3HT possesses a mobility approximately  $10^{-4} \text{ cm}^2 \text{ V}^{-1} \text{ s}^{-1}$  for holes, but P3HT's electron mobility is many orders of magnitude lower, approximately  $10^{-8} \text{ cm}^2 \text{ V}^{-1} \text{ s}^{-1}$  [49]. Conversely, the archetypal OPV fullerene derivative PCBM possesses high electron mobility (approximately  $10^{-3} \text{ cm}^2 \text{ V}^{-1} \text{ s}^{-1}$ ) but a much lower hole mobility (approximately  $10^{-8} \text{ cm}^2 \text{ V}^{-1} \text{ s}^{-1}$ ) [50].

Given this material selectivity of carrier mobility, in our simulations we choose spatially dependent carrier mobilities from the local composition by

$$\mu_n(x, y) = 10^{\tilde{\mu}_{n,D} + (\tilde{\mu}_{n,A} - \tilde{\mu}_{n,D})C_A(x,y)}, \quad (17)$$

where  $\mu_n$  is the electron mobility at spatial position  $(x, y)$ ,  $\tilde{\mu}_{n,A/D}$  is the order of magnitude of the mobility of electrons moving among a network of pure acceptor or donor molecules, and  $C_A(x, y)$  is the compositional profile of the active layer. We add the additional subscript to the compositional morphology term generated from Eq. (15) to make explicit that we define  $C_A(x, y) = 1$  as corresponding to pure electron acceptor material (i.e., the fullerene derivative). We define the spatially varying hole mobility in a similar fashion. With this functional form, the carrier mobility can vary several orders of magnitude at different spatial positions, as determined by the local composition. We choose this functional form specifically so that the mixed interfacial region possesses a moderate degree of carrier mobility, which is at an order of magnitude somewhere in between that of the two pure components. We justify this choice based on the logic that a mixed region should have an appreciable charge-carrier mobility due to the presence of the appropriate conducting molecule in that region. However, since these regions also tend to be amorphous and contain the other nonconducting component, it follows that the mixed region should be less conductive than the pure phase.

It should be noted that there are technically two different approaches for mapping mobilities onto the mixed-phase domains in the interfacial regions: either by first smoothing the compositional morphology and then mapping the charge-carrier mobilities (our chosen method), or an alternate method where the mobility mapping is performed first and then the mobility profiles are subsequently smoothed. With the first method, which we choose to implement, the carrier mobilities in the mixed region tend to be over an order of magnitude smaller than those in the pure phases (representing the geometric average of the two) with large fluctuations depending on the exact composition. In contrast, the alternative mapping-before-smoothing approach produces mobilities in the mixed phase that are all roughly about one-half that in the pure phases (the arithmetic average) with relatively little compositional fluctuations. At least one study shows that thermal annealing (which generally enhances phase segregation) leads to an increase of mobility by several orders of magnitude, which we attribute to the reduction of forced charge transport through mixed phases [51]. As the exact experimental values of carrier mobilities in the mixed phase are unknown, for the major part of this study, we choose to focus on the smoothing-before-mapping approach since this produces mixed-phase mobilities that are most in agreement with experimental values. However, we explore both approaches for mobility mapping, and examples illustrating how the different approaches yield different device performance trends are given in the Supplemental Material [52].

One additional morphology-dependent feature that should affect charge transport is the HOMO and LUMO energy levels of the conducting materials. The exact numerical values of the molecular energy levels of the mixed-composition phase and their impact on device performance is an area of active research [53–55]. Our goal in this work is not to include every possible detail in our simulated OPV devices but rather to choose a consistent realistic model for which we can controllably tune the degree of mixing to see how the resulting device behavior changes. Nonetheless, we also simulate the morphological impact of the components' energy levels on device performance by implementation of a hopping model for charge transport across internal interfaces [56,57] and then study the effects of mixing on top of the variable-energy hopping. Although there are some quantitative and qualitative differences between the results with and without variable-energy hopping, we find that the inclusion of energy levels does not affect our general conclusion that the introduction of a mixed phase may be both beneficial and deleterious to device performance. This suggests that a simple mapping of composition to mobility is sufficient to capture the impact of an interfacial mixed phase on device performance, and, thus, we focus on the more simple simulations for the remainder of this paper. The results and details of our variable-energy hopping simulations may be found in the Supplemental Material [52].

Finally, we note that recent work by van Duren *et al.* shows that films that contain only acceptors and mixed phase (i.e., devices that are predominantly fullerene with little polymer) also can function well as the active layer in organic photovoltaic devices [58]. We also apply our DD modeling to better understand the role of the mixed phase in this class of devices. We find, consistent with experiment, that the absence of the pure polymer phase provides little hindrance to device performance; the details of these simulations and our analysis can also be found in the Supplemental Material [52].

#### 4. Transfer-matrix approach for calculating carrier generation profiles

To determine the carrier generation profile to be used in our simulations, we begin with a transfer-matrix calculation using an effective-medium approximation to calculate the wavelength-dependent absorption profile through the device based on the AM1.5 spectrum [38]. This absorption profile determines where excitons are generated. Charge carriers, however, are generated by the absorption of light only if the resulting excitons on the absorbing donor are subsequently split at a donor-acceptor interface. In other words, charge carriers should be generated predominantly in proximity to the interface between the two components of both of our experimental and Cahn-Hilliard morphologies. It is well established that excitons have a diffusion length of approximately 5–10 nm in most OPV material blends [59]. Thus, we expect carrier generation to be maximized at the interfaces between the binary phases and to decay in magnitude moving outward from that interface.

To account for the preferential generation of free charges near the donor-acceptor interface in our simulations, we first determine the mesh points of our binarized morphology that represent the location of the interface between donor and acceptor materials. The generation of carriers should be highest at these mesh points (i.e., the exciton dissociation efficiency equals 1). The adjacent and proximal mesh points are then assigned exponentially decaying efficiency of exciton dissociation radiating outward from the interface, such that no excitons should be split within an approximate 10-nm region around the interface. We then convolve this exponentially decaying profile with the transfer-matrix absorption profile, resulting in a spatially dependent carrier generation profile that properly accounts for both morphological and exciton diffusion effects. An example of such a generation profile for a CH morphology with an average feature size of approximately 10 nm is presented in Fig. 1. This method for generation rate profile determination is different than that applied in the experimental HAADF STEM morphology. With that morphology, the generation of charges is set to occur only in regions that are specifically characterized as mixed phase. When we apply the same exponential generation profile mapping method as is utilized for the CH morphologies to the

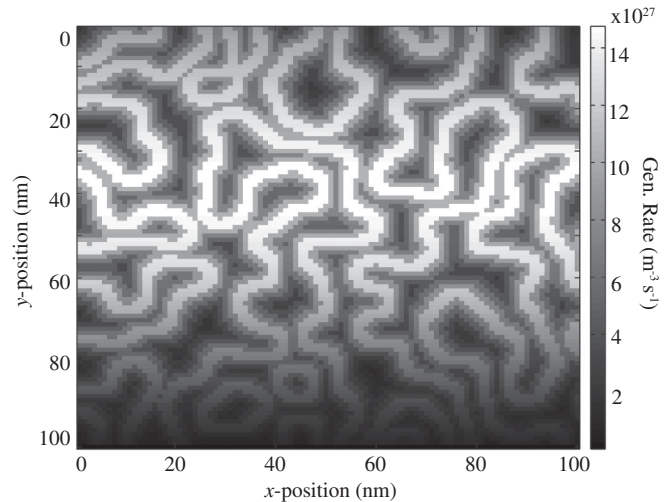


FIG. 1. An example of a spatially dependent generation rate for a morphology generated by Cahn-Hilliard modeling for the morphology presented in Fig. 2. Charge carriers are generated only in proximity to the interface between the donor and acceptor phases.

experimental morphology, we see minimal differences in the calculated device performance between the two methods. A discussion of the different generation profile mapping techniques as applied to the experimental morphology is presented in the Supplemental Material [52].

### III. RESULTS AND DISCUSSION

#### A. Simulations with only pure-component domains

##### 1. Cahn-Hilliard-generated morphologies

Before we begin our analysis of the effects of a mixed-composition domain on OPV charge transport, we start by investigating a series of binarized (i.e., only pure domains) device morphologies, so that we may better understand how the presence of a mixed phase either helps or hinders device performance. We start by simulating the  $J$ - $V$  characteristic of the binarized Cahn-Hilliard-generated morphologies by solving Eqs. (3)–(5) as a function of applied voltage bias (the full  $J$ - $V$  characteristics are presented in the Supplemental Material [52]). We present an example of one such morphology in Fig. 2. Specifically, the presented images refer to a CH morphology with an average domain size of approximately 10 nm. We present snapshots of the morphology at varying degrees of mixing: first when only pure-component domains are present [0% mixing, Fig. 2(a)] and the same morphology with two different levels of Gaussian smoothing that result in 30% [Fig. 2(b)] and 70% [Fig. 2(c)] mixing of the active layer. The color map for these images is such that white corresponds to pure acceptor material (i.e., fullerene), and black corresponds to pure donor material (i.e., polymer). The orientation is such that the top of the image corresponds to the transparent anode, and the bottom corresponds to the metallic cathode. After

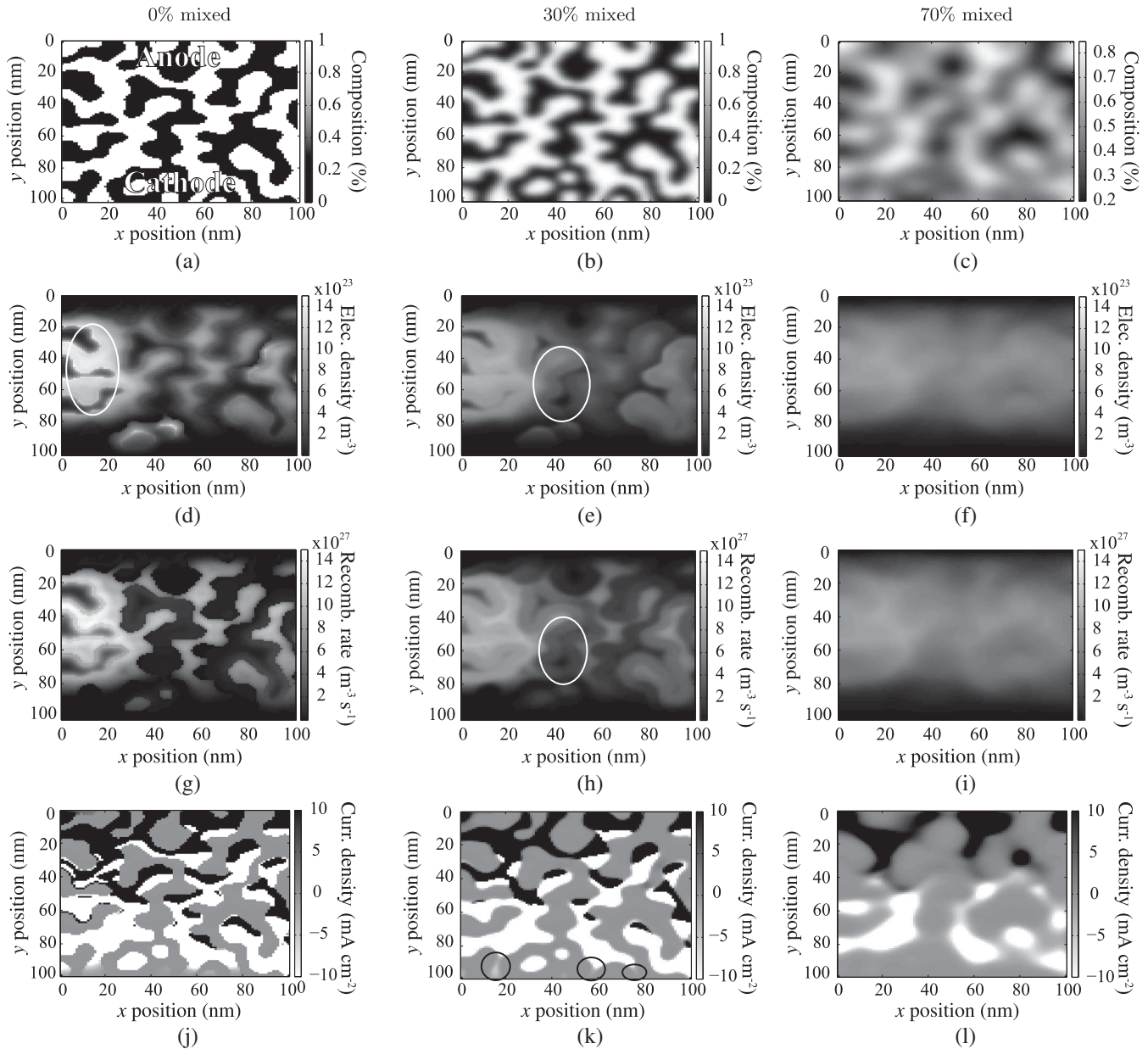


FIG. 2. Simulation results of OPV devices based on CH morphologies with a controllably increasing amount of intermixed-compositional regions from left (no intermixing) to right (most intermixing). All figures represent the device at short-circuit conditions under simulated AM1.5 illumination. (a)–(c) overall compositional morphology; (d)–(f) spatially dependent electron density; (g)–(i) spatially dependent recombination rate; (j)–(l) electron current-density profile. Each of these image plots shows a  $100 \times 100 \text{ nm}^2$  subsection of the entire simulated device. The ITO/PEDOT:PSS anode and the calcium cathode are located at the top and bottom of each plot, respectively. The three columns correspond to devices with 0%, 30%, and 70% of the active area characterized as mixed phase, respectively. The circled regions in panels (d), (e), (h), and (k) highlight various bottlenecks and other morphological effects on the device electronic behavior that are discussed in the text.

mapping this initial morphology to mobility and generation profiles as described above, we solve Eqs. (3)–(5) and simulate the  $J$ - $V$  characteristic measurement for each morphology. The steady-state position-dependent solutions for the electron density, the recombination rate of carriers, and the  $y$  (vertical) component electron current density ( $n$ ,  $R$ , and  $J_{n,y}$ ) at 0-V applied bias (built-in field only) are also presented in the second, third, and fourth rows of Fig. 2, respectively.

Although our simulations are inherently two dimensional, we follow the common convention of assuming that the observables are uniform in the third dimension and present the carrier densities and recombination rates in units of  $(\text{m}^{-3})$  instead of  $(\text{m}^{-2})$ . Similarly, we present the current density as a flux in units of  $(\text{A m}^{-2})$ .

Immediately apparent from the carrier density plot in Fig. 2(d) is how indirect conduction pathways and

morphological traps result in significant charge accumulation at various points through the device; the white oval in Fig. 2(d) highlights one such region with significant charge accumulation. The large regions of charge accumulation like the one highlighted are characterized by both high carrier generation (i.e., near the interface between pure domains) and the lack of a direct continuous conductive pathway between the generation site and the electron extraction cathode (the cathode is located at the bottom of the figure in our representation). In these regions, electrons are forced to either slowly drift through the pure polymer phase, diffuse against the built-in electric field to find a less resistive pathway, or be lost to recombination. Perhaps not surprising, these regions of accumulated charge are also localized regions with an increased rate of charge-carrier recombination, as presented in Fig. 2(g).

## 2. Empirical (HAADF STEM) morphology

To validate that our simulations of Cahn-Hilliard-generated morphologies are qualitatively representative of an actual BHJ morphology, we also simulate the  $J$ - $V$  characteristic of a morphology determined by HAADF STEM microscopy. We present the same set of observables that are examined for the CH morphologies ( $C_A$ ,  $n$ ,  $R$ , and  $J_{n,y}$ ) in Fig. 3. The same phenomena observed in the CH morphologies are evident in the HAADF STEM morphology. The tortuous charge-transport pathways of the morphology result in charge accumulation at various points inside the device, particularly when charges are generated without a direct pathway towards their preferred extraction electrode (again, for electrons, the cathode is located at the bottom of the figure). The accumulation of charge results in increased rates of recombination at localized regions of the device's morphology. We note that there is also significant leakage current of electrons at the anode (so-called surface recombination), as the accumulation of charges and tortuous pathways causes electrons to diffuse to and be extracted at the “wrong” metal contact.

All of these phenomena result in a rather poorly performing device with a power-conversion efficiency of 0.616%, a result of possessing a  $J$ - $V$  characteristic with a  $J_{SC}$  of  $3.38 \text{ mA cm}^{-2}$ , a  $V_{OC}$  of 0.642 V, and a fill factor (FF) of 0.409 (see the Supplemental Material [52] for the full  $J$ - $V$  characteristic). Unfortunately, there is no experimentally determined  $J$ - $V$  characteristic for this morphology since the sample is specifically fabricated to obtain tomographic data, which involves either the removal of or the complete lack of a top metal contact. In other words, although this empirical morphology is meant to represent real BHJ device films, it is *not* a functional OPV device. However, OPV devices fabricated from these same materials typically exhibit much higher device performance than what we observe in our simulations [60]. This low performance is likely the result of an unusually coarse (large domain sizes)

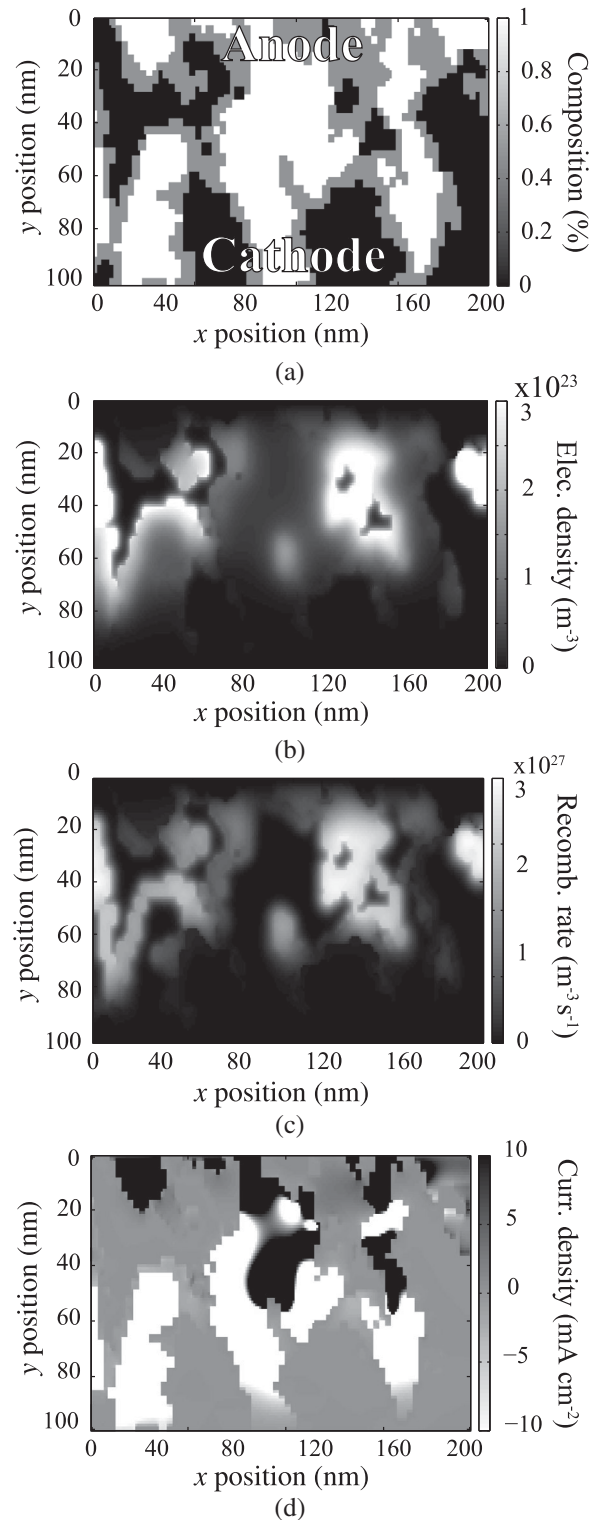


FIG. 3. Image plots of simulation data for an experimentally determined (by HAADF STEM) BHJ morphology taken from Ref. [18]. Panels (a)–(d) present the compositional morphology, steady-state electron density, steady-state recombination rate, and the  $y$  component (vertical component) of the electron current-density vector, respectively, all presented under short-circuit conditions (i.e., at 0-V applied bias). The images show the data for the central  $100 \times 200 \text{ nm}^2$  subsection of the full morphology.

subsection of the full morphology as well as the fact that we are considering only charge transport in 2D. In a real 3D device, there will be additional transport pathways in the  $z$  dimension (which we do not consider) so that the 3D morphology will be less restrictive to charge transport. However, the qualitative agreement of the key simulated observables ( $n$ ,  $R$ , and  $J_{n,y}$ ) between the CH morphologies and the HAADF STEM morphology suggests that the results and conclusions drawn from our computer-generated morphologies are a reasonable approximation of those in real OPV devices.

## B. Simulations with different degrees of mixed phase

### 1. Charge densities and recombination rates

With this basic description of how a disordered morphology with only pure domains impacts an OPV's charge-transport properties in hand, we now examine the effects of introducing an interfacial mixed-phase domain. The images in the middle and right-hand columns in Fig. 2 show the spatially dependent electron density and recombination rate at different degrees of mixing for our approximately 10-nm CH morphology with the simulated device held at short-circuit conditions under AM1.5G illumination. As discussed in Sec. III A 1, the presence of morphological traps in devices without a mixed phase results in regions of charge accumulation, which, in turn, result in locally increased recombination rates. In the center panels of Fig. 2, we see that when this same morphology is smoothed to become 30% mixed, there is an overall drop in the steady-state charge density. In particular, the charge density is reduced in the dead-end regions that previously exhibited higher amounts of recombination. Figure 2(h) shows that the introduction of the mixed phase also reduces the peak recombination rates. Note that although the average carrier density and recombination rate decrease when the mixed phase is introduced, there are some regions of the device (particularly regions that were originally pure donor material) that actually exhibit an increase in carrier density and local recombination rate [indicated by the circled regions of Figs. 2(e) and 2(h)].

This trend of increased charge density in certain regions persists to higher degrees of mixing, as illustrated by the right-hand panels in Fig. 2. Figures 2(f) and 2(i) show that there is an overall increase in charge density and recombination throughout the device as the degree of mixing is increased to 70%. At this point, the amorphous mixed region dominates charge transport through the active layer. Most of the fine structural details originally present at lower degrees of mixing are lost as the morphology becomes more like that of a homogeneous medium. At this extreme, although charge accumulation is lessened in some areas, most regions of the active layer see increased charge density. The increase in charge density and recombination rate due to the redistribution of charges from morphological dead ends into the amorphous mixed regions results in an

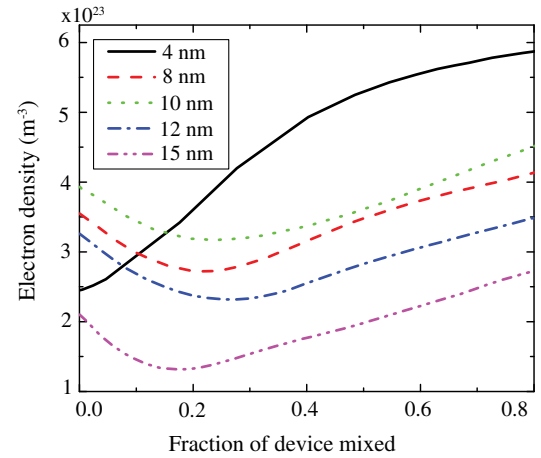


FIG. 4. Average electron density of the five different Cahn-Hilliard BHJ morphologies at varying degrees of mixing. Although most morphology length scales exhibit a drop and subsequent rise in electron density with increased mixing, the 4-nm device exhibits a rise in electron density because additional mixing leads directly to constriction of the conduction pathways.

overall drop in device performance; overmixing appears to constrict formerly conducting pure-component pathways by lowering the local mobility, as we discuss in more detail in Sec. III C. The trends for the average electron density for all of our CH morphology domain sizes as a function of mixing are presented in Fig. 4. We see similar trends for most domain sizes as that for the approximate 10-nm morphology explored in Fig. 2, where charge density decreases upon initial mixing but then increases at higher levels of mixing. Of particular note is that the charge density of the 4-nm device increases only upon mixing of the two components. It appears that at this feature size, there are already many conducting pathways and almost no morphological traps. As such, the introduction of mixing does nothing to ease choke points and dead ends so that the debilitating effects of overmixing become manifest immediately.

### 2. Conducting pathways

So far, it appears that the introduction of a mixed-phase region most directly affects charge transport by either reducing the severity of dead ends that trap carriers or by constricting previously existing pure-phase conducting pathways. These effects are more evident when examining the electron current-density profiles of active layers with varying degrees of mixing, which are shown in Figs. 2(j)–2(l). For the sake of clarity, we present only the  $y$  component of the electron current-density vector,  $J_{n,y}$ . The color map scale is such that white corresponds to electrons flowing down towards the cathode, while black corresponds to electrons flowing up towards the anode. Note that the tortuous morphology prevents many electrons from being extracted from the device, and there is

significant leakage current in proximity of the anode, which reduces the resulting photocurrent.

In the nonmixed morphology [Fig. 2(j)], there are more occurrences of leakage current throughout the device, particularly at dead ends and far upstream of high-conductivity pathways. At these points, charge carriers are unable to drift towards the cathode and instead must reverse direction to either find a new conduction pathway or leak out of the device at the anode (so-called “surface recombination”) [61]. These points of current “reversal” appear to be exacerbated by the abrupt interface between conducting phases. Upon the introduction of an interfacial mixed-phase region, Fig. 2(k), there is an immediate drop in leakage current and current reversal near structural dead ends: clearly, charges are able to flow through the device with less obstruction from the morphology with the addition of a modest amount of mixed phase. This improvement in charge transport is manifest in the device’s increased fill factor and  $J_{SC}$ , which we illustrate in Sec. III C. However, at higher levels of mixing, Fig. 2(l), the high-conductivity pathways are narrowed, particularly in proximity to the cathode [cf. the circled regions in Fig. 2(k)]. Transport through the mixed phase then becomes the limiting factor for device performance as carriers slowly traverse through the less conductive amorphous region and increasingly constricted pure-phase conduction channels.

It appears that this balance and interplay between the amelioration of dead ends and the narrowing of high-current channels is more pronounced for simulated morphologies with larger average feature sizes. In the case of morphologies with a 4-nm average feature size, the bicontinuous network is already effectively strongly mixed compared to the dimensions of the device, resulting in a preponderance of conducting pathways, despite the absence of an explicitly mixed region. Although the introduction of a mixed phase may reduce some of the dead ends in the device, the many conducting pathways of this device are also significantly constricted (see the Supplemental Material [52]). This constriction occurs at a lower degree of mixing than for the coarser morphologies, partly because the pure-phase conduction pathways of the 4-nm morphology are already fairly narrow to begin with. Thus, morphologies with domain sizes of approximately 4 nm are so susceptible to conduction-channel narrowing that the introduction of an interfacial mixed phase is immediately detrimental to device performance.

### C. Effects of mixed phase on device performance

We now understand in general terms how the presence of a mixed phase may both improve and hinder charge transport through a BHJ active layer by either easing morphological traps or narrowing conducting channels. With this understanding, we turn in this section to exploring precisely how the introduction of a mixed phase affects photovoltaic device performance. In Fig. 5, we illustrate the

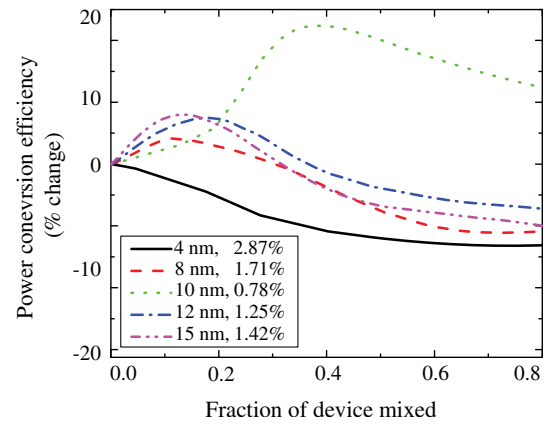


FIG. 5. Change in the power-conversion efficiency of five Cahn-Hilliard-generated BHJ morphologies with different intrinsic separation length scales studied as a function of the degree of mixing of the two pure phases; the efficiencies quoted in the legend are those of the unmixed devices.

effect of introducing different amounts of interfacial mixing on the PCE of simulated devices with different average domain sizes. The figure plots the percent variation of the devices’ PCEs from their value in the absence of any mixed phase so that the effects of mixing can be compared for BHJs with the pure phases separated on different length scales. The absolute values of the simulated devices’ power-conversion efficiencies and other figures of merit are given in Table III.

The results show that most of the morphologies we study exhibit an initial improvement in power-conversion efficiency upon the introduction of mixed-composition interfacial regions. However, this improvement in PCE does not persist at higher degrees of mixing, and it is clear that the performance of overly mixed devices suffers, dropping below the devices’ original PCE. For most of the morphology length scales we test, the peak in device performance occurs when the mixed phase accounts for approximately 15%–20% of the devices’ total active area. However, the 10-nm length-scale morphology, which benefits the most from mixing, reaches its peak performance at approximately 45% mixed phase with nearly double the unmixed power-conversion efficiency.

TABLE III. The initial absolute figures of merit for simulated devices without any mixed-composition phase present.

Average domain size	PCE (%)	$J_{SC}$ (mA cm <sup>-2</sup> )	FF	$V_{OC}$ (V)
4 nm	2.87	−9.43	0.510	0.690
8 nm	1.71	−4.71	0.562	0.677
10 nm	0.783	−4.00	0.425	0.639
12 nm	1.25	−3.56	0.550	0.685
15 nm	1.42	−3.21	0.600	0.722
Experimental morphology	0.616	−3.38	0.409	0.642

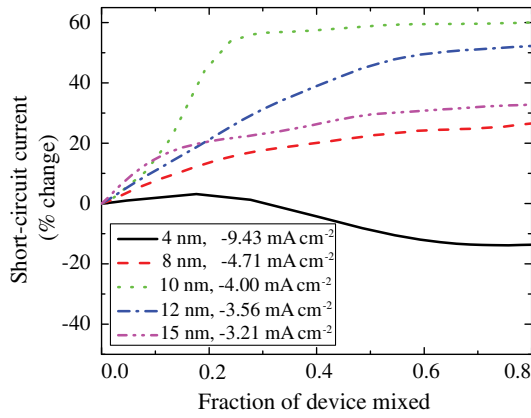


FIG. 6. Change in the short-circuit current of five Cahn-Hilliard-generated BHJ morphologies with different intrinsic separation length scales studied as a function of the degree of mixing of the two pure phases; the  $J_{SC}$ 's quoted in the legend are those of the unmixed devices.

And as discussed above, when the average feature size is very small, as with the 4-nm feature-size morphology, the addition of any interfacial mixed phase hinders the performance of the device, with the overall efficiency dropping by approximately 50% as the already finely mixed BHJ's transport properties become increasingly dominated by the mixed phase.

### 1. Short-circuit current ( $J_{SC}$ )

To better understand how the interplay between the degree of mixing and the overall device morphology affect device performance, in Fig. 6 we plot the change in  $J_{SC}$  of our simulated devices as a function of the degree of mixing. As with the trend in PCE, most of the devices'  $J_{SC}$ 's improve upon the introduction of a mixed phase. Unlike the trend for PCE, however, most of the simulated devices'  $J_{SC}$ 's reach a plateau after their initial increase, rather than decreasing at higher degrees of mixing. The point at which this plateau occurs is slightly different for each device morphology length scale, but most of the devices appear to reach their  $J_{SC}$  plateau at approximately 15%–35% mixed phase.

The one exception to this plateau behavior is the simulated devices with 4-nm average feature size, which show only a very small increase in  $J_{SC}$  with increased mixing before dropping below the original unmixed value. This is because the finely structured BHJ possesses relatively few morphological traps, so the introduction of a mixed phase is detrimental to charge transport as the highly conducting pure phases are narrowed. For the coarser morphologies (greater than 8-nm average domain size), there are enough morphological traps such that mixing initially improves the  $J_{SC}$  by smoothing these traps away, but at higher degrees of mixing, this improvement is counteracted by the narrowing of the pure-phase

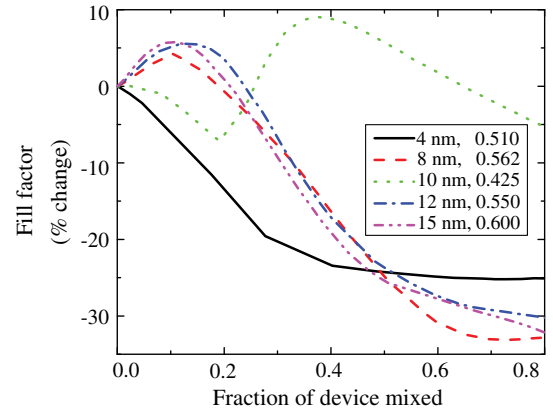


FIG. 7. Percent change in the fill factor of five Cahn-Hilliard-generated BHJ morphologies with different intrinsic separation length scales studied as a function of the degree of mixing of the two pure phases; the FFs quoted in the legend are those of the unmixed devices.

conducting channels, accounting for the plateau in  $J_{SC}$  of these devices upon further mixing.

### 2. Fill factor

Figure 7 shows that the FFs of our simulated devices each exhibit different trends depending on their morphological length scale upon the introduction of different amounts of interfacial mixed-composition phase. The BHJs with phase separation on larger length scales (8, 12, and 15 nm) follow a similar trend as seen for the overall device performance: an initial improvement followed by a significant drop at higher levels of mixing. As previously noted, for the 4-nm CH morphology, which has very few initial morphological traps, the introduction of a mixed phase serves only to constrict the devices' conducting pathways, which manifest as a lower fill factor.

The BHJ with the 10-nm morphology, however, exhibits an unusual and nonmonotonic trend with increased mixing. The active layer with the 10-nm average size scale initially follows the same trend as the 4-nm device, in that its fill factor drops. However, with increased mixing, the 10-nm BHJ morphology's fill factor experiences a sharp rise, peaks, and then drops off again. This unusual trend can be understood by examining the structural changes that occur in BHJs with this length-scale morphology upon mixing [Figs. 2(a)–2(c)]. The 10-nm length-scale BHJ initially possess several long relatively straight conduction channels for electrons (white, connected segments). There are also several isolated regions of acceptor material (left portion of each panel) that do not allow for proper electron transport. A small degree of mixing hinders the FF because mixing of this morphology leads to narrowing of the conducting pathways. However, as the size of the mixed phase is increased, previously separated conducting segments become connected, creating new conduction pathways that restore carrier balance and improve the FF, until at higher

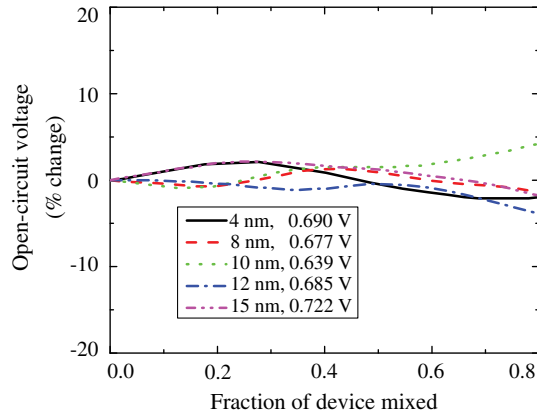


FIG. 8. Percent change in the open-circuit voltages of five Cahn-Hilliard-generated BHJ morphologies with different intrinsic separation length scales studied as a function of the degree of mixing of the two pure phases; the  $V_{OC}$ 's quoted in the legend are for the unmixed devices.

degrees of mixing, the eventual blurring of the conductive pathways ultimately decreases device performance. All of this illustrates how random variations in an OPV's active-layer morphology can have a major and unexpected impact on device its performance, and why there has been so much discussion in the literature about precisely how much a mixed phase is optimum.

### 3. Open-circuit voltage ( $V_{OC}$ )

The last figure of merit of note for OPV devices is the open-circuit voltage. The  $V_{OC}$  is the applied bias necessary to counteract the flow of charge from the built-in electric field. This means that near  $V_{OC}$ , drift currents are minimized, so any variation in  $V_{OC}$  resulting from the introduction of interfacial mixed phase should be manifest primarily via diffusion current effects in the DD model. The diffusion current, however, is limited by the mobility of charge carriers, and the mobility of the carriers in OPVs is quite low regardless of the degree of mixing. As such, we expect that the introduction of a mixed phase should have only a small effect on a BHJ device's  $V_{OC}$ .

Our simulations support this reasoning, as illustrated in Fig. 8. For all morphology length scales, the introduction of a mixed interfacial region has minimal effect on the simulated devices'  $V_{OC}$ . There are some minor fluctuations, particularly for the morphologies with the smallest and largest feature sizes. However, these fluctuations are less than approximately 5% and are much smaller than the more drastic changes exhibited by the other device figures of merit. The relative nondependence of an OPV device's  $V_{OC}$  on active-layer morphological features, such as the presence of a mixed phase, is in line with our previous work that shows little effect of structural disorder on the device open-circuit voltage [34].

## IV. CONCLUSIONS

With this study we illustrate that the mixed-composition phase can have both beneficial and detrimental effects on the overall performance of polymer/fullerene BHJ photovoltaic devices. Kinetic Monte Carlo simulations by Jones *et al.* [14] have previously suggested that the introduction of a mixed phase should lead to diminished device performance. However, those simulations considered only two classes of BHJ morphologies: those with only pure donor and acceptor domains and those with pure fullerene aggregates suspended in a mixed-phase matrix. The authors of that study asserted that ternary-phase BHJs (those with pure donor-acceptor domains and a mixed interfacial phase) should exhibit device performance intermediate between the two binary-phase morphologies. While our drift-diffusion simulations similarly show that an excessive amount of mixed phase does indeed diminish device performance, we find that a moderate amount of mixing may, in fact, lead to increased device performance. On the one hand, the mixed phase can, to an extent, reduce the tortuosity of a morphology that is obstructive to charge transport by reducing dead ends and creating new conduction pathways, leading to improved performance. We observe this effect in both our Cahn-Hilliard-generated morphologies as well as our single empirical morphology, although the empirical morphology is considerably coarser (approximately 26-nm average domain size) than any of our CH morphologies and may not be fully representative of typical BHJs. However, at higher degrees of mixing, overall device performance suffers as conduction pathways are constricted and charges are forced to transport through the relatively less conducting mixed phase. The point at which the mixed phase switches from helping to hindering device performance depends on the average feature size and the connectivity of the device's morphology. When there are relatively few morphological traps, as is the case for our simulated 4- and 10-nm average-feature-size devices, the introduction of a mixed phase offers little benefit, since there are few traps to ameliorate. However, as is seen with the 10-nm device, the introduction of a mixed phase can also allow for the creation of new conduction pathways between regions previously separated by nonconducting material. This shows that a mixed phase may have significant effects depending on the exact details of a device's morphology.

It is worth emphasizing that the greatest improvement in overall device efficiency is exhibited by the device with a 10-nm length-scale morphology. This is the typical morphological length scale assumed to comprise most BHJ-type solar cells. This suggests that the presence of a mixed phase plays a significant role in the charge-transport properties of high-performing BHJ devices and may be necessary for optimum device performance of organic solar cells. That said, it is important to realize that the impact of a mixed-composition interfacial phase on an OPV device's

performance is highly nonmonotonic. Since different donor-acceptor blends exhibit different phase-separation kinetics and degrees of mixing in a uncontrollable way, it is highly likely that the performance impact of the mixed phase is one of the root causes of the difficulty involved with optimizing new OPV donor-acceptor blends for device performance. This suggests that new fabrication techniques, such as sequential processing of donor-acceptor materials [62], are required to manipulate and control the degree of mixing in BHJ devices in a reproducible manner.

### ACKNOWLEDGMENTS

The authors acknowledge support from the National Science Foundation under Grants No. CHE-1112569 and No. CBET-1510353.

- [1] Jing-De Chen, Chaohua Cui, Yan-Qing Li, Lei Zhou, Qing-Dong Ou, Chi Li, Yongfang Li, and Jian-Xin Tang, Single-junction polymer solar cells exceeding 10% power conversion efficiency, *Adv. Mater.* **27**, 1035 (2015).
- [2] Abd. Rashid bin Mohd Yusoff, Dongcheon Kim, Hyeong Pil Kim, Fabio Kurt Schneider, Wilson Jose da Silva, and Jin Jang, A high efficiency solution processed polymer inverted triple-junction solar cell exhibiting a power conversion efficiency of 11.83%, *Energy Environ. Sci.* **8**, 303 (2015).
- [3] Deborah Leman, Mary Allison Kelly, Stuart Ness, Sebastian Engmann, Andrew Herzog, Chad Snyder, Hyun Wook Ro, R. Joseph Kline, Dean M. DeLongchamp, and Lee J. Richter, *In situ* characterization of polymer fullerene bilayer stability, *Macromolecules* **48**, 383 (2015).
- [4] Wei-Ru Wu, U-Ser Jeng, Chun-Jen Su, Kung-Hwa Wei, Ming-Shin Su, Mao-Yuan Chiu, Chun-Yu Chen, Wen-Bin Su, Chiu-Hun Su, and An-Chung Su, Competition between fullerene aggregation and poly(3-hexylthiophene) crystallization upon annealing of bulk heterojunction solar cells, *ACS Nano* **5**, 6233 (2011).
- [5] Christoph J. Brabec, Martin Heeney, Iain McCulloch, and Jenny Nelson, Influence of blend microstructure on bulk heterojunction organic photovoltaic performance, *Chem. Soc. Rev.* **40**, 1185 (2011).
- [6] Paul Westacott, John R. Tumbleston, Safa Shoaee, Sarah Fearn, James H. Bannock, James B. Gilchrist, Sandrine Heutz, John deMello, Martin Heeney, Harald Ade, James Durrant, David S. McPhail, and Natalie Stingelin, On the role of intermixed phases in organic photovoltaic blends, *Energy Environ. Sci.* **6**, 2756 (2013).
- [7] Benjamin Schmidt-Hansberg, Michael F.G. Klein, K. Peters, Felix Buss, J. Pfeifer, S. Walheim, Alexander Colsmann, Uli Lemmer, P. Scharfer, and W. Schabel, *In situ* monitoring the drying kinetics of knife coated polymer-fullerene films for organic solar cells, *J. Appl. Phys.* **106**, 124501 (2009).
- [8] Ye Huang, Edward J. Kramer, Alan J. Heeger, and Guillermo C. Bazan, Bulk heterojunction solar cells: Morphology and performance relationships, *Chem. Rev.* **114**, 7006 (2014).
- [9] E. Buchaca-Domingo *et al.*, Additive-assisted supramolecular manipulation of polymer:fullerene blend phase morphologies and its influence on photophysical processes, *Mater. Horiz.* **1**, 270 (2014).
- [10] Bingyuan Huang, Jojo A. Amonoo, Anton Li, X. Chelsea Chen, and Peter F. Green, Role of domain size and phase purity on charge carrier density, mobility, and recombination in poly(3-hexylthiophene):phenyl-c61-butyric acid methyl ester devices, *J. Phys. Chem. C* **118**, 3968 (2014).
- [11] Jonathan A. Bartelt, Zach M. Beiley, Eric T. Hoke, William R. Mateker, Jessica D. Douglas, Brian A. Collins, John R. Tumbleston, Kenneth R. Graham, Aram Amassian, Harald Ade, Jean M. J. Fréchet, Michael F. Toney, and Michael D. McGehee, The importance of fullerene percolation in the mixed regions of polymer-fullerene bulk heterojunction solar cells, *Adv. Energy Mater.* **3**, 364 (2013).
- [12] Wing C. Tsoi, Steve J. Spencer, Li Yang, Amy M. Ballantyne, Patrick G. Nicholson, Alan Turnbull, Alex G. Shard, Craig E. Murphy, Donal D.C. Bradley, Jenny Nelson, and Ji-Seon Kim, Effect of crystallization on the electronic energy levels and thin film morphology of P3HT:PCBM blends, *Macromolecules* **44**, 2944 (2011).
- [13] A. Bruno, L. X. Reynolds, C. Dyer-Smith, J. Nelson, and S. A. Haque, Determining the exciton diffusion length in a polyfluorene from ultrafast fluorescence measurements of polymer/fullerene blend films, *J. Phys. Chem. C* **117**, 19832 (2013).
- [14] Matthew L. Jones, Reesha Dyer, Nigel Clarke, and Chris Groves, Are hot charge-transfer states the primary cause of efficient free-charge generation in polymer:fullerene organic photovoltaic devices? A kinetic Monte Carlo study, *Phys. Chem. Chem. Phys.* **16**, 20310 (2014).
- [15] Wei-Ru Wu, U-Ser Jeng, Chun-Jen Su, Kung-Hwa Wei, Ming-Shin Su, Mao-Yuan Chiu, Chun-Yu Chen, Wen-Bin Su, Chiu-Hun Su, and An-Chung Su, Competition between fullerene aggregation and poly(3-hexylthiophene) crystallization upon annealing of bulk heterojunction solar cells, *ACS Nano* **5**, 6233 (2011).
- [16] G. Li, Y. Yao, H. Yang, V. Shrotriya, G. Yang, and Y. Yang, "Solvent annealing" effect in polymer solar cells based on poly(3-hexylthiophene) and methanofullerenes, *Adv. Funct. Mater.* **17**, 1636 (2007).
- [17] Youngkyoo Kim, Stelios A. Choulis, Jenny Nelson, Donal D. C. Bradley, Steffan Cook, and James R. Durrant, Device annealing effect in organic solar cells with blends of regioregular poly(3-hexylthiophene) and soluble fullerene, *Appl. Phys. Lett.* **86**, 063502 (2005).
- [18] Olga Wodo, John D. Roehling, Adam J. Moule, and Baskar Ganapathysubramanian, Quantifying organic solar cell morphology: A computational study of three-dimensional maps, *Energy Environ. Sci.* **6**, 3060 (2013).
- [19] Wei Chen, Maxim P. Nikiforov, and Seth B. Darling, Morphology characterization in organic and hybrid solar cells, *Energy Environ. Sci.* **5**, 8045 (2012).
- [20] Stefan D. Oosterhout, Martijn M. Wienk, Svetlana S. van Bavel, Ralf Thiedmann, L. Jan Anton Koster, Jan Gilot, Joachim Loos, Volker Schmidt, and René a.J. Janssen, The effect of three-dimensional morphology on the efficiency of hybrid polymer solar cells, *Nat. Mater.* **8**, 818 (2009).

- [21] Wolfgang Tress, Karl Leo, and Moritz Riede, Optimum mobility, contact properties, and open-circuit voltage of organic solar cells: A drift-diffusion simulation study, *Phys. Rev. B* **85**, 155201 (2012).
- [22] Inchan Hwang and Neil C. Greenham, Modeling photocurrent transients in organic solar cells, *Nanotechnology* **19**, 424012 (2008).
- [23] Florent Monestier, Jean-Jacques Simon, Philippe Torchio, Ludovic Escoubas, François Flory, Sandrine Bailly, Remi de Bettignies, Stéphane Guillerez, and Christophe Defranoux, Modeling the short-circuit current density of polymer solar cells based on P3HT:PCBM blend, *Sol. Energy Mater. Sol. Cells* **91**, 405 (2007).
- [24] Klára Maturová, Svetlana S. van Bavel, Martijn M. Wienk, René A. J. Janssen, and Martijn Kemerink, Morphological device model for organic bulk heterojunction solar cells, *Nano Lett.* **9**, 3032 (2009).
- [25] W. Geens, T. Martens, J. Poortmans, T. Aernouts, J. Manca, L. Lutsen, P. Heremans, S. Borghs, R. Mertens, and D. Vanderzande, Modelling the short-circuit current of polymer bulk heterojunction solar cells, *Thin Solid Films* **451–452**, 498 (2004).
- [26] Young Min Nam, June Huh, and Won Ho Jo, Optimization of thickness and morphology of active layer for high performance of bulk-heterojunction organic solar cells, *Sol. Energy Mater. Sol. Cells* **94**, 1118 (2010).
- [27] Klára Maturová, Svetlana S. van Bavel, Martijn M. Wienk, René A. J. Janssen, and Martijn Kemerink, Description of the morphology dependent charge transport and performance of polymer:fullerene bulk heterojunction solar cells, *Adv. Funct. Mater.* **21**, 261 (2011).
- [28] Biswajit Ray, Pradeep R. Nair, and Muhammad A. Alam, Annealing dependent performance of organic bulk-heterojunction solar cells: A theoretical perspective, *Sol. Energy Mater. Sol. Cells* **95**, 3287 (2011).
- [29] Biswajit Ray and Muhammad A. Alam, Random vs regularized OPV: Limits of performance gain of organic bulk heterojunction solar cells by morphology engineering, *Sol. Energy Mater. Sol. Cells* **99**, 204 (2012).
- [30] James C. Blakesley and Dieter Neher, Relationship between energetic disorder and open-circuit voltage in bulk heterojunction organic solar cells, *Phys. Rev. B* **84**, 075210 (2011).
- [31] Thomas Kirchartz, Bart E. Pieters, James Kirkpatrick, Uwe Rau, and Jenny Nelson, Recombination via tail states in polythiophene:fullerene solar cells, *Phys. Rev. B* **83**, 115209 (2011).
- [32] C. M. Martin, V. M. Burlakov, and H. E. Assender, Modeling charge transport in composite solar cells, *Sol. Energy Mater. Sol. Cells* **90**, 900 (2006).
- [33] Adam Raba, Anne-Sophie Cordan, and Yann Leroy, Two-dimensional simulation of organic bulk heterojunction solar cell: Influence of the morphology, *J. Nanosci. Nanotechnol.* **13**, 5164 (2013).
- [34] Benjamin Y. Finck and Benjamin J. Schwartz, Drift-Diffusion Modeling of the Effects of Structural Disorder and Carrier Mobility on the Performance of Organic Photovoltaic Devices, *Phys. Rev. Applied* **4**, 034006 (2015).
- [35] Olga Wodo and Baska Ganapathysubramanian, Modeling morphology evolution during solvent-based fabrication of organic solar cells, *Comput. Mater. Sci.* **55**, 113 (2012).
- [36] Christopher M. Snowden, *Semiconductor Device Modeling* (Peter Peregrinus Ltd., Piscataway, New Jersey, 1988).
- [37] Evelyn Knapp, Roger Häusemann, H. U. Schwarzenbach, and Beat Ruhstaller, Numerical simulation of charge transport in disordered organic semiconductor devices, *J. Appl. Phys.* **108**, 054504 (2010).
- [38] Leif A. A. Pettersson, Lucimara S. Roman, and Olle Inganäs, Modeling photocurrent action spectra of photovoltaic devices based on organic thin films, *J. Appl. Phys.* **86**, 487 (1999).
- [39] Hermann K. Gummel, Self-consistent iterative scheme for 1-dimensional steady state transistor calculations, *IEEE Trans. Electron Devices* **11**, 455 (1964).
- [40] Donald L. Scharfetter and Hermann K. Gummel, Large-signal analysis of a silicon read diode oscillator, *IEEE Trans. Electron Devices* **16**, 64 (1969).
- [41] Siegfried Selberherr, *Analysis and Simulation of Semiconductor Devices* (Springer, New York, 1984), pp. 208–212.
- [42] J. Campbell Scott and George G. Malliaras, Charge injection and recombination at the metal-organic interface, *Chem. Phys. Lett.* **299**, 115 (1999).
- [43] Inchan Hwang, Christopher R. McNeill, and Neil C. Greenham, Drift-diffusion modeling of photocurrent transients in bulk heterojunction solar cells, *J. Appl. Phys.* **106**, 094506 (2009).
- [44] David J. Eyre, An unconditionally stable one-step scheme for gradient systems, <http://www.math.utah.edu/~eyre/research/methods/stable.ps>; MATLAB code, <http://www.math.utah.edu/~eyre/computing/matlab-intro/ch.txt>.
- [45] Lukasz Bolikowski and Maria Gokieli, in *Parallel Processing and Applied Mathematics*, edited by Roman Wyrzykowski, Jack Dongarra, Konrad Karczewski, and Jerzy Waśniewski (Springer, Berlin, 2014), pp. 510–519; MATLAB code, <https://github.com/bolo1729/cahn-hilliard>.
- [46] Hari K. Kodali and Baskar Ganapathysubramanian, A computational framework to investigate charge transport in heterogeneous organic photovoltaic devices, *Comput. Methods Appl. Mech. Eng.* **247–248**, 113 (2012).
- [47] Gavin A. Buxton and Nigel Clarke, Predicting structure and property relations in polymeric photovoltaic devices, *Phys. Rev. B* **74**, 085207 (2006).
- [48] Benjamin P. Lyons, Nigel Clark, and Chris Groves, The relative importance of domain size, domain purity and domain interfaces to the performance of bulk-heterojunction organic photovoltaics, *Energy Environ. Sci.* **5**, 7657 (2012).
- [49] Christian Melzer, Erik J. Koop, Valentin D. Mihailetschi, and Paul W.M. Blom, Hole transport in poly (phenylene vinylene)/methanofullerene bulk-heterojunction solar cells, *Adv. Funct. Mater.* **14**, 865 (2004).
- [50] Frédéric Laquai, Denis Andrienko, Ralf Mauer, and Paul W. M. Blom, Charge carrier transport and photogeneration in P3HT:PCBM photovoltaic blends, *Macromol. Rapid Commun.* **36**, 1001 (2015).
- [51] V. D. Mihailetschi, H. X. Xie, B. de Boer, L. J. A. Koster, and P. W. M. Blom, Charge transport and photocurrent generation in poly (3-hexylthiophene): Methanofullerene bulk-heterojunction solar cells, *Adv. Funct. Mater.* **16**, 699 (2006).

- [52] See Supplemental Material at <http://link.aps.org/supplemental/10.1103/PhysRevApplied.6.054008> for details on Cahn-Hilliard simulations, alternate mobility and generation mapping methods, consideration of local molecular-energy levels, and additional morphologies.
- [53] Chris Groves, Suppression of geminate charge recombination in organic photovoltaic devices with a cascaded energy heterojunction, *Energy Environ. Sci.* **6**, 1546 (2013).
- [54] Sean Sweetnam, Rohit Prasanna, Timothy M. Burke, Jonathan A. Bartelt, and Michael D. McGehee, How the energetic landscape in the mixed phase of organic bulk heterojunction solar cells evolves with fullerene content, *J. Phys. Chem. C* **120**, 6427 (2016).
- [55] T. M. Clarke and J. R. Durrant, Charge photogeneration in organic solar cells, *Chem. Rev.* **110**, 6736 (2010).
- [56] Allen Miller and Elihu Abrahams, Impurity conduction at low concentrations, *Phys. Rev.* **120**, 745 (1960).
- [57] B. Ruhstaller, S. A. Carter, S. Barth, H. Riel, W. Riess, and J. C. Scott, Transient and steady-state behavior of space charges in multilayer organic light-emitting diodes, *J. Appl. Phys.* **89**, 4575 (2001).
- [58] Jeroen K. J. van Duren, Xiaoniu Yang, Joachim Loos, Corrie W. T. Bulle-Lieuwma, Alexander B. Sieval, Jan C. Hummelen, and René A. J. Janssen, Relating the morphology of poly (p-phenylene vinylene)/methanofullerene blends to solar-cell performance, *Adv. Funct. Mater.* **14**, 425 (2004).
- [59] Oleksandr V. Mikhnenko, Hamed Azimi, Markus Scharber, Mauro Morana, Paul W. M. Blom, and Maria Antonietta Loi, Exciton diffusion length in narrow bandgap polymers, *Energy Environ. Sci.* **5**, 6960 (2012).
- [60] Moritz Liedtke, Andreas Sperlich, Hannes Kraus, Andreas Baumann, Carsten Deibel, Maarten J. M. Wirix, Joachim Loos, Claudia M. Cardona, and Vladimir Dyakonov, Triplet exciton generation in bulk-heterojunction solar cells based on endohedral fullerenes, *J. Am. Chem. Soc.* **133**, 9088 (2011).
- [61] Christopher M. Proctor and Thuc-Quyen Nguyen, Effect of leakage current and shunt resistance on the light intensity dependence of organic solar cells, *Appl. Phys. Lett.* **106**, 083301 (2015).
- [62] Jordan C. Aguirre, Steven A. Hawks, Amy S. Ferreira, Patrick Yee, Selvam Subramaniyan, Samson A. Jenekhe, Sarah H. Tolbert, and Benjamin J. Schwartz, Sequential processing for organic photovoltaics: Design rules for morphology control by tailored semi-orthogonal solvent blends, *Adv. Energy Mater.* **5**, 1402020 (2015).